Strategic intercalation of AB$_2$O$_4$ perovskite oxides for synergistic enhanced redox activity in sulphonated Ti$_3$C$_2$T$_x$ MXene for energy storage applications

Jitesh Pani[a,b], Priyanka Chaudhary[b], Hitesh Borkar*[a], Meng-Fang Lin*[b]

[a]*Department of Physics, National Institute of Technology, Warangal, Telangana 506004, India*

[b]*Department of Materials Engineering, Ming Chi University of Technology, New Taipei City 24301, Taiwan*

Corresponding author email: bhitesh@nitw.ac.in, mflin@mail.mcut.edu.tw
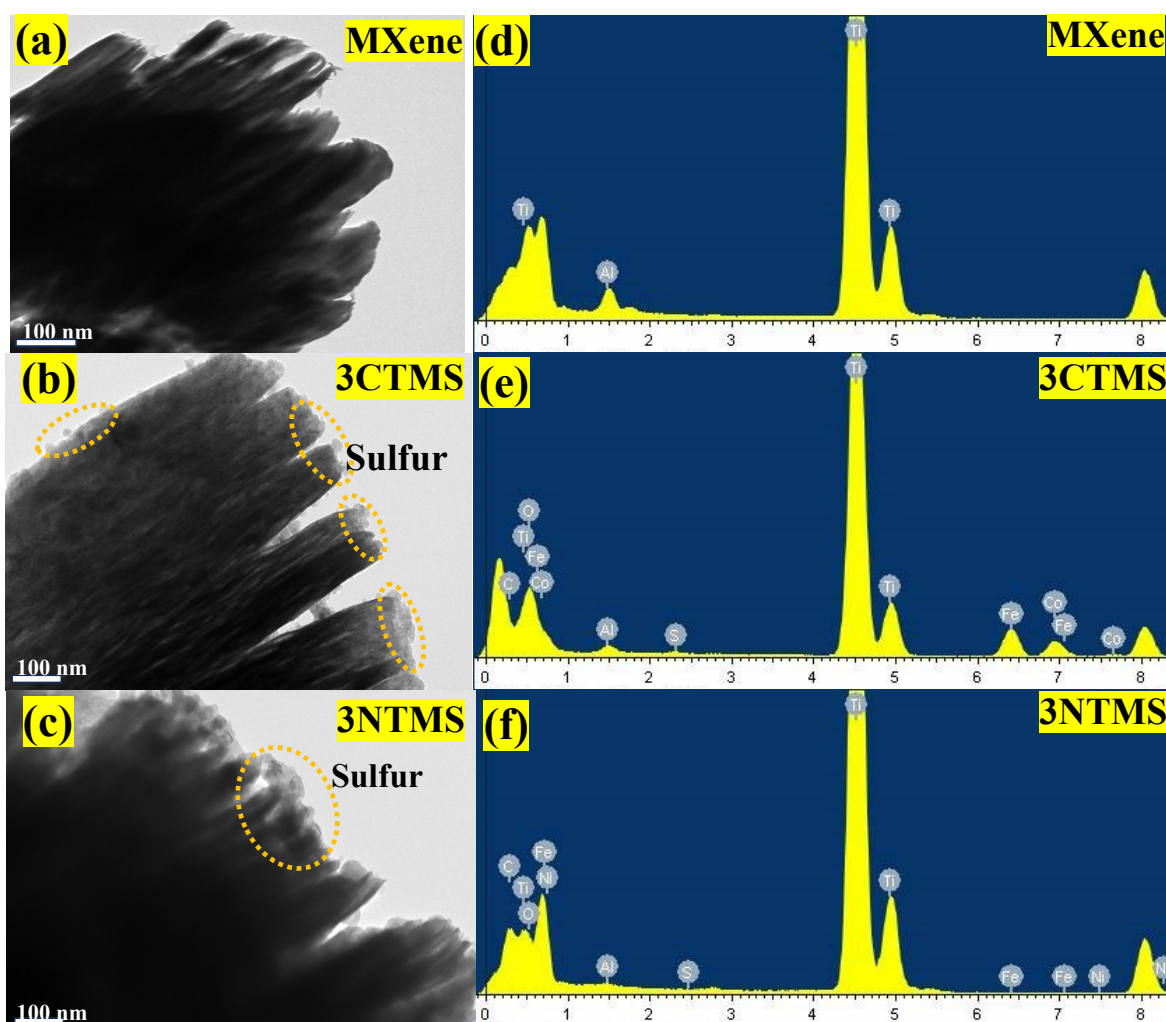
Supporting Information

Fig. S1 TEM image of (a) TMS, (b) 3CTMS and (c) 3NTMS showing the presence of sulphur. EDS analysis of 3CTMS, TEM image of (d) TMS, (e) 3CTMS and (f) 3NTMS.

From **Fig. S2**a, the Ti_3AlC_2 MAX phase is presented, which consists of alternating Ti-C and Al layers, forming a lamellar structure. This lamellar structure suggests tight packing between layers due to the metallic bonds connecting them.[1] After removal of Al layer from MAX phase, **Fig. S2**b shows the successful formation of Ti-C layered structure, leading to formation of TM. The sulphonation of MXene morphology is evident in **Fig. S2**c, which shows successfully sulphonated sheets with sulfur particles on the surface of MXene, indicating the presence of -SO_3H bond attached to the surface of layered sheets. A micrograph at 1μm magnification has been included in the inset of **Fig. S2c** to verify uniformity and delamination of sheets in TMS. The intercalation of CFO particles into the TMS layered sulphonated surface at 3, 5 and 7 wt% are presented in **Fig. S2**d, e and f, respectively. The successful insertion of NFO nanoparticles with 3, 5 and 7 wt% into the layered structure of TMS are presented in **Fig. S2**g, h and i, respectively. The elemental mapping of 3CTMS shown in **Fig. S3** confirms the sulphonation of the surface of MXene. **Fig. S3**e represents the S ion attached all throughout the surface. **Fig. S3**c, g and h confirm the presentence of O, Fe and Co (Elements from $CoFe_2O_4$) at the similar sites of S ion.

To have a more qualitative understanding of CFO and NFO particle insertion and elemental composition, point- Energy-dispersive X-ray (point- EDAX) analysis was carried out. Spectrum 1 in **Fig. S4**a represents the point EDAX at TMS surface whose elemental composition in terms of atomic % and mass % have been provided in table (Right hand top side)1.37 mass % of S denotes the sulphonation of the MXene surface. Spectrum 2 in **Fig. S4**b represents the point EDAX at an inserted nanoparticle within the TMS surface whose elemental composition in terms of atomic % and mass % have been provided in table (Right hand bottom side). The dominant percentage of Co, Fe and O in spectrum 2 confirms the intercalation of CFO within the layered TMS. The spectrum labeled Spectrum 1 in **Fig. S5**a corresponds to the EDAX point at TMS surface. The elemental composition is provided in terms of both atomic percentage and mass percentage in the table located on the right-hand

top side. Point EDAX at a nanoparticle visible at the layered surface has been provided in **Fig. S5**b. The intercalation of NFO within the layered TMS was confirmed by prevalent proportion Ni, Fe and O as shown in table corresponding to Spectrum 2.

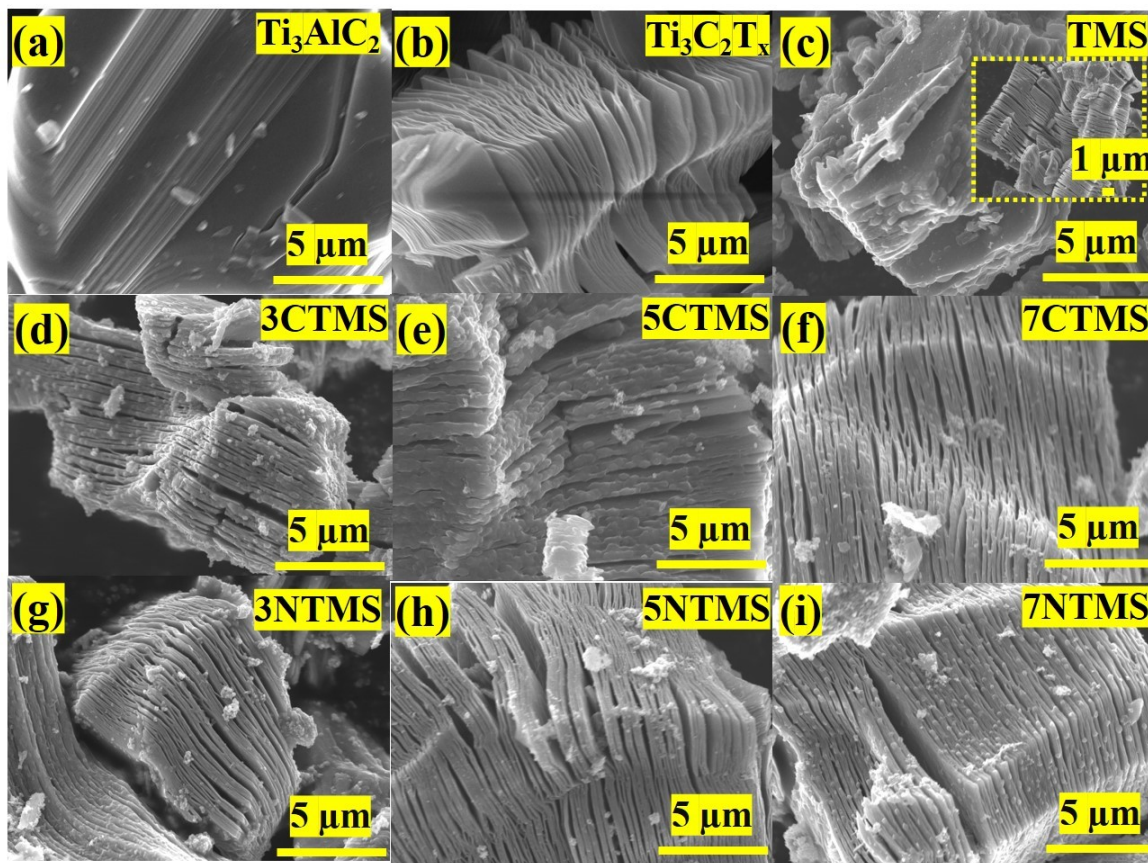
Fig. S2 FESEM images of (a) Ti_3AlC_2 MAX phase, (b) $Ti_3C_2T_x$ MXene, (c) MXene with DMSO (Inset- Micrograph at 1μm), (d) 3CTMS, (e) 5CTMS, (f) 7CTMS, (g) 3NTMS, (h) 5NTMS and (i) 7 NTMS at 5μm magnification.
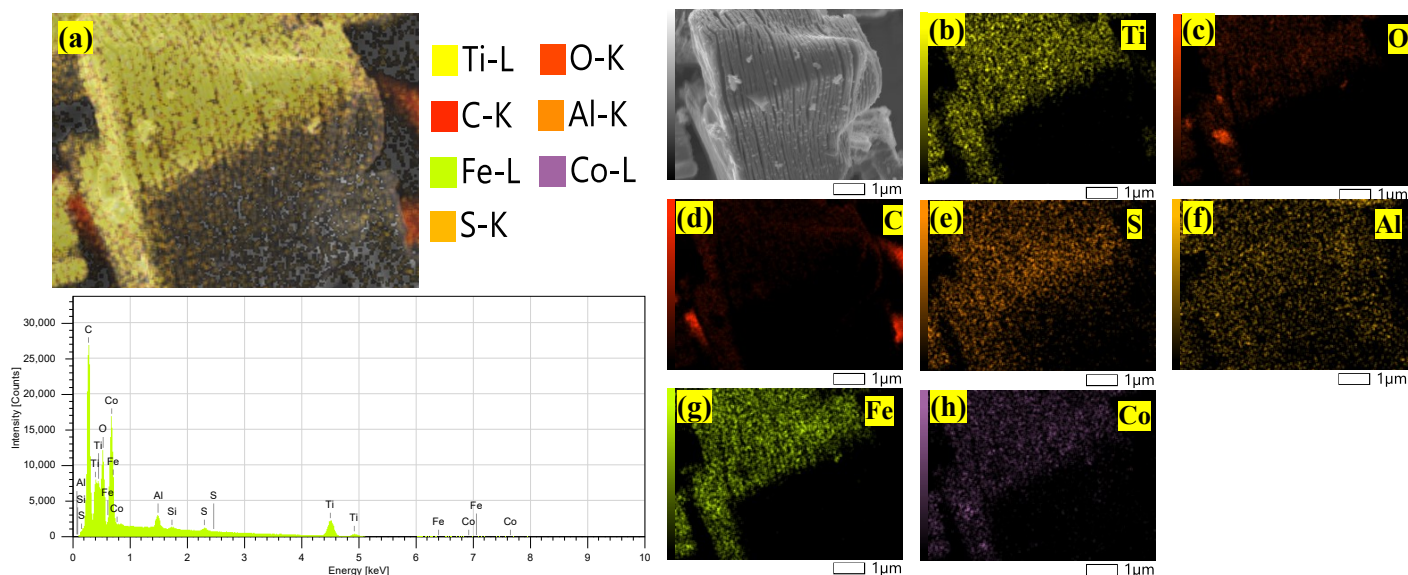
Fig. S3 Elemental mapping of 3CTMS, showing (a) the presence of all detected elements with their intensity distribution represented in the accompanying graph, and individual mappings for (b) Ti, (c) O, (d) C, (e) S, (f) Al, (g) Fe and (h) Co.
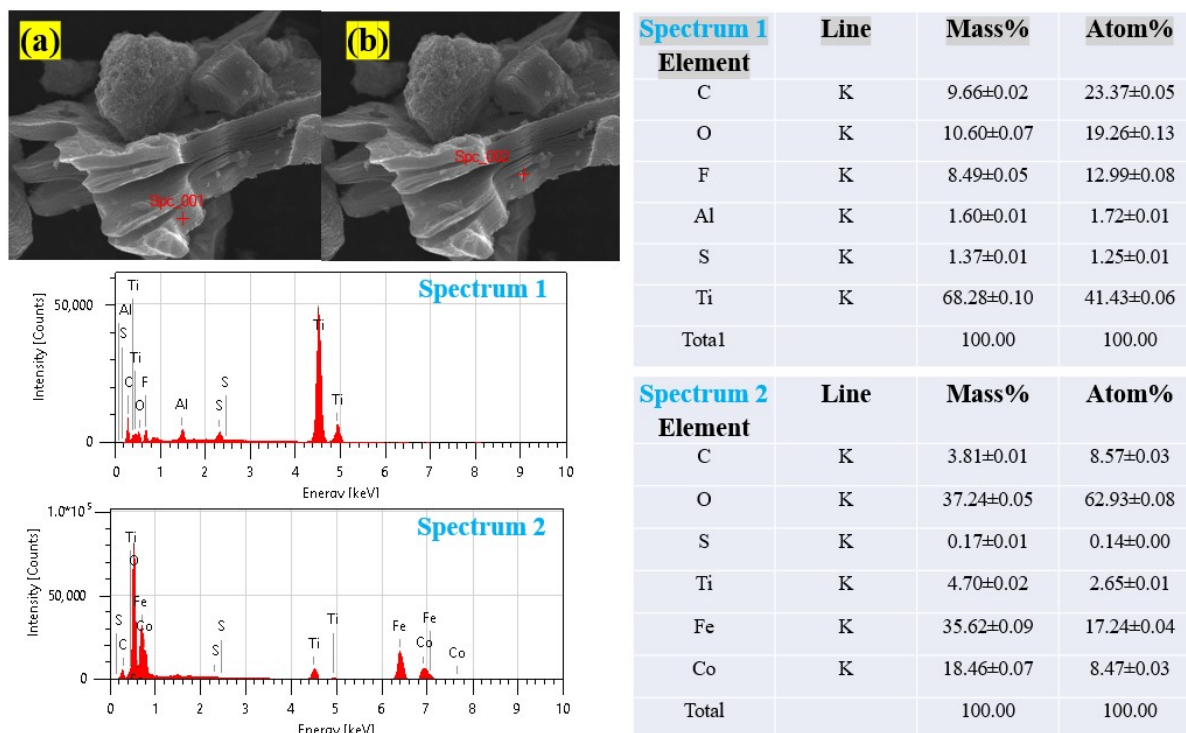

Spectrum 1 Element	Line	Mass%	Atom%
C	K	9.66±0.02	23.37±0.05
O	K	10.60±0.07	19.26±0.13
F	K	8.49±0.05	12.99±0.08
Al	K	1.60±0.01	1.72±0.01
S	K	1.37±0.01	1.25±0.01
Ti	K	68.28±0.10	41.43±0.06
Total		100.00	100.00

Spectrum 2 Element	Line	Mass%	Atom%
C	K	3.81±0.01	8.57±0.03
O	K	37.24±0.05	62.93±0.08
S	K	0.17±0.01	0.14±0.00
Ti	K	4.70±0.02	2.65±0.01
Fe	K	35.62±0.09	17.24±0.04
Co	K	18.46±0.07	8.47±0.03
Total		100.00	100.00

Fig. S4 Point EDAX at two locations in 3CTMS sample: (a) Spectrum 1 showing the elemental composition of the MXene sheet (elemental percentage given in the table at the top right), (b) Spectrum 2 showing the elemental composition of $CoFe_2O_4$ (elemental percentage given in table at the bottom right).

Spectrum 1 Element	Line	Mass%	Atom%
C	K	15.33±0.02	31.81±0.05
O	K	9.52±0.05	14.83±0.08
F	K	17.02±0.06	22.33±0.07
Al	K	1.72±0.02	1.59±0.02
S	K	0.36±0.02	0.28±0.01
Ti	L	56.36±0.26	29.15±0.13
Total		100.00	100.00

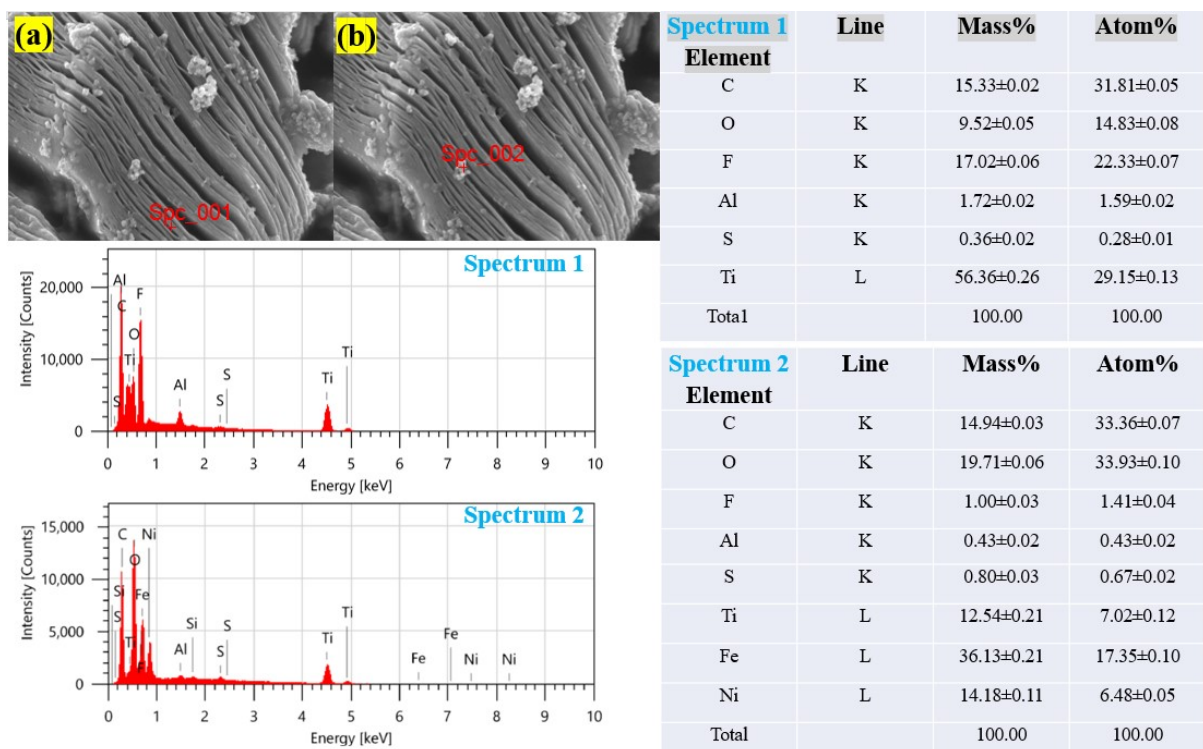| Spectrum 2 Element	Line	Mass%	Atom%
C	K	14.94±0.03	33.36±0.07
O	K	19.71±0.06	33.93±0.10
F	K	1.00±0.03	1.41±0.04
Al	K	0.43±0.02	0.43±0.02
S	K	0.80±0.03	0.67±0.02
Ti	L	12.54±0.21	7.02±0.12
Fe	L	36.13±0.21	17.35±0.10
Ni	L	14.18±0.11	6.48±0.05
Total		100.00	100.00

Fig. S5 Point EDAX at two locations in the 3NTMS sample: (a) Spectrum 1 showing elemental composition of the MXene sheet (elemental percentage given in the table at the top right), (b) Spectrum 2 showing the elemental composition of $NiFe_2O_4$ (elemental percentage given in the tablea at the bottom right).
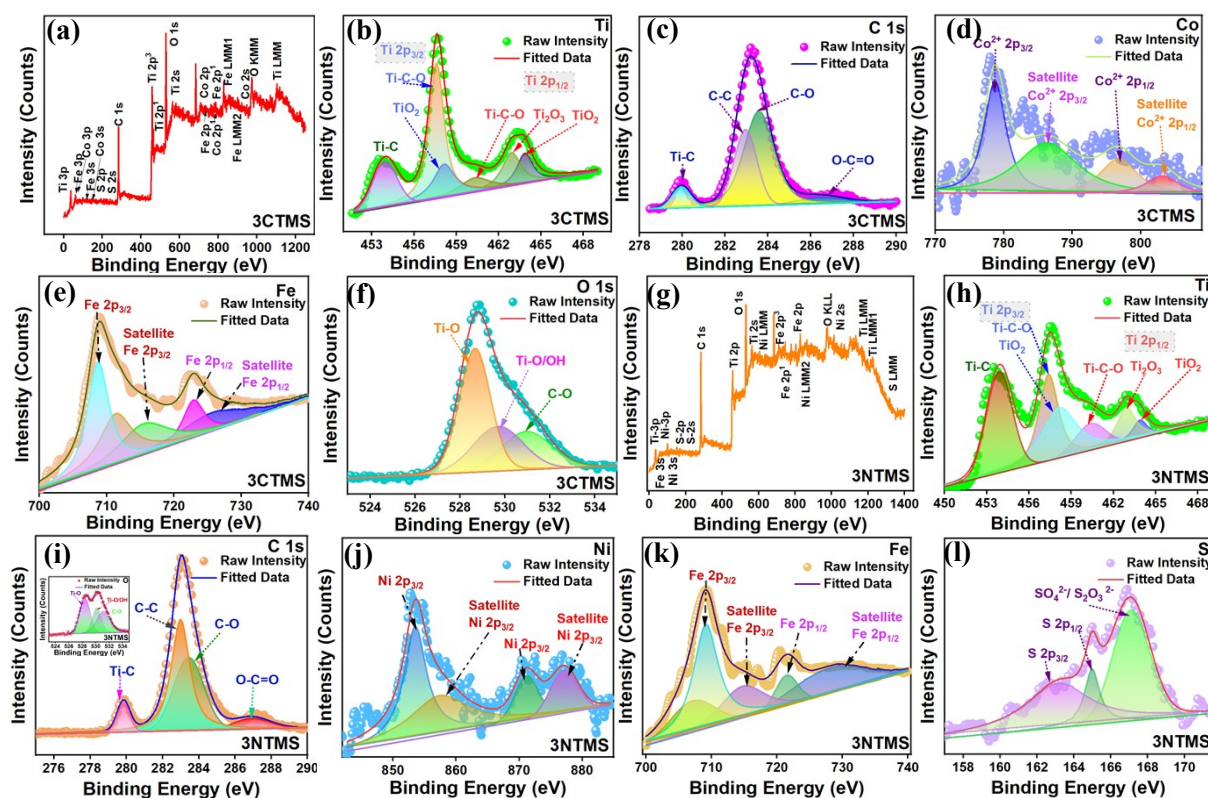
Fig. S6 XPS survey spectra of (a) 3CTMS, with detailed XPS spectra for (b) Ti, (c) C 1s, (d) Co, (e) Fe, (g) O1s in 3CTMS. XPS survey spectra of (g) 3NTMS, with detailed XPS spectra for (h) Ti, (i) C 1s (Inset- O Spectra), (j) Ni, (k) Fe, (l) S in 3NTMS.

Fig. S6a shows the survey XPS spectra of 3CTMS, confirming the presence of Ti 2p, O1s, Fe 2p, Co 2p, C 1s and S 2s. A comparison of XPS peak assignments and corresponding areas for 3CTMS and 3NTMS is provided in **Table S1**. **Fig. S6**b demonstrates the high-resolution XPS spectrum of Ti with fitting results peaks at 457.59 and 460.3 eV corresponding to Ti-C-O (Ti $2p_{3/2}$) and Ti-C-O (Ti $2p_{1/2}$), respectively. Peaks at binding energies 453.9 and 462.9 eV correspond to Ti-C and Ti_2O_3 bonds [2]. Additionally, peaks at 458.13 and 463.8 eV are assigned to TiO_2 (Ti $2p_{3/2}$) and TiO_2 (Ti $2p_{1/2}$), respectively, which align with previously reported results.[3] Based on binding energy, the deconvoluted C 1s spectrum shows fitted peaks for Ti-C, C-C, C-O and O-C=O at 279.57, 282.95, 283.58 and 286.46 eV, respectively. The presence of Ti-C and O-C=O confirms the incorporation of CFO within TMS. **Fig. S6**d, e and f show the high resolution XPS spectra for Co, Fe and O, respectively, in the CFO phase. The Co spectrum shows peaks corresponding to $Co^{2+}2p_{3/2}$, Satellite $Co^{2+}2p_{3/2}$, $Co^{2+}2p_{1/2}$ and Satellite $Co^{2+}2p_{1/2}$ at 778.71, 796.8, 786.3 and 803.2 eV, respectively. [4,5] The Co^{2+} oxidation state, as obtained from XPS, indicates successful CFO formation, stable under MXene and DMSO sonication process. **Fig. S6**e shows the XPS spectra for Fe 2p. Oxidation states of Fe 2p are indicated to be Fe $2p_{3/2}$ and Fe $2p_{1/2}$ at 708.712 and 722.89 eV, respectively. Peaks at 711.35 and 725.77 eV ascribed to oscillating satellite peaks for Fe $2p_{3/2}$ and Fe $2p_{1/2}$, respectively. Ti-O, Ti-O/OH and C-O constitutional chemical species of O are observed at 528.66, 529.69 and 530.95 eV as shown in **Fig. S6**f. The existence of Ti 2p, O1s, Fe 2p, Ni 2p, C 1s and S 2s have been evidenced in survey spectrum of 3NTMS as presented in **Fig. S6**b. **Fig. S6**h demonstrates the high-resolution spectra of Ti and its fitting where the peaks at 457.388 and 460.370 eV corresponds to Ti-C-O (Ti $2p_{3/2}$)

and Ti-C-O (Ti $2p_{1/2}$), respectively. Peaks at binding energy 453.89 and 462.91 eV indicates the presence of Ti-C and Ti_2O_3 bonds [2]. Peaks at 458.170 and 463.88 eV are assigned to TiO_2 (Ti $2p_{3/2}$) and TiO_2 (Ti $2p_{1/2}$), respectively which are consistent with previously reported results.[3] The sulphonation of MXene surfaceis confirmed by the sharp S peaksin **Fig. S6**l. Based on binding energy, the deconvoluted fitted peaks of C 1s shows Ti-C, C-C, C-O and O-C=O at 279.84 282.99, 283.44, 286.94 and 778.71 eV, respectively (**Fig. S6**i). Ti-O, Ti-O/OH and C-O constitutional chemical species of O are observed at 528.40, 530.14 and 531.11 eV as shown in inset of **Fig. S6**i. The Ni^{2+} oxidation state as obtained in XPS is responsible for successful NFO formation and stable under MXene and DMSO sonication process.[6] **Fig. S6**j presents the high resolution XPS spectra of Ni indicating the existence of Ni $2p_{3/2}$ and Ni $2p_{1/2}$ at 853.33 and 873.5 eV, respectively.[7] The satellite peaks coordinating with Ni $2p_{3/2}$ and Ni $2p_{1/2}$ exists at 855.7 and 878.44 eV, respectively. [8] **Fig. S6**k shows the XPS spectra for Fe 2p, with oxidation states of Fe 2p indicated byFe $2p_{3/2}$ and Fe $2p_{1/2}$ at 707.08 and 721.45 eV. Peaks at 709.16 and 714.9 eV ascribed to oscillating satellite peaks for Fe $2p_{3/2}$ and Fe $2p_{1/2}$, respectively. Peaks at 163.162 and 164.985 eV corresponds to S $2p_{3/2}$ and S $2p_{1/2}$, respectively. [9] The sulphonation of the MXene surface is confirmed through presence of $SO_4^{2-}/S_2O_3^{2-}$ peak as shown in **Fig. S6**l. The peak position of this state in the composition is at 167.36 eV well in agreement with previously reported data confirming $SO_4^{2-}/S_2O_3^{2-}$ states. [10]

Table S1. Binding energies and peak areas of 3CTMS and 3NTMS in XPS spectra

S. No.	Element	Bonding	Peak Position, BE (eV)		% Area	
			3CTMS	3NTMS	3CTMS	3NTMS
1	Ti	Ti-C	453.93	453.89	8094.92	10955.72
2		Ti-C-O (Ti $2p_{3/2}$)	457.59	457.38	20194.03	9062.4
3		TiO_2 (Ti $2p_{3/2}$)	458.13	458.17	7739.52	10007.43
4		Ti-C-O (Ti $2p_{1/2}$)	460.3	460.37	4428.18	3356.77
5		Ti_2O_3	462.9	462.91	6337.12	3637.12
6		TiO_2 (Ti $2p_{1/2}$)	463.8	463.88	4795.11	1480.29
7	S	**S $2p_{3/2}$**	**162.51**	**163.16**	**77.99**	**405.18**
8		**S $2p_{1/2}$**	**165.54**	**164.98**	**168.36**	**118.97**
9		**SO_4^{2-} /$S_2O_3^{2-}$**	**167.3**	**167.1**	**388.64**	**391.96**
10	C	Ti-C	279.95	279.84	1142.14	1408.48
11		C-C	282.95	282.9	5219.38	10852.22
12		C-O	283.58	283.44	10198.47	8461.61
13		O-C=O	286.46	286.9	908.1	1465.39
14	Co	Co^{2+} $2p_{3/2}$	778.71	-	2823.52	-
15		Co^{2+} $2p_{1/2}$	796.8	-	1503.81	-
16		Satellite Co^{2+} $2p_{3/2}$	786.3	-	3511.03	-
17		Satellite Co^{2+} $2p_{1/2}$	803.2	-	698.73	-
18	Fe	Fe $2p_{3/2}$	708.71	707.08	4277.34	1269.78
19		Satellite Fe $2p_{3/2}$	711.35	709.12	3261.45	3407.71
20		Satellite Fe $2p_{1/2}$	715.48	714.9	2686.8	1507.04
21		Fe $2p_{1/2}$	722.89	721.45	1436.64	628.82

22		Satellite Fe 2p$_{1/2}$	725.77	725.83	2172.85	1650.52
23	O	Ti-O	528.66	528.4	17666	12507.74
24		Ti-O/OH	529.69	530.14	9780.99	9112.06
25		C-O	530.95	531.11	8450.63	11016.67
26	Ni	Ni 2p$_{3/2}$	-	853.33	-	1133.53
27		Satellite Ni 2p$_{3/2}$	-	855.7	-	4106.93
28		Ni 2p$_{1/2}$	-	873.500	-	2901.037
29		Satellite Ni 2p$_{1/2}$	-	878.448	-	397.912
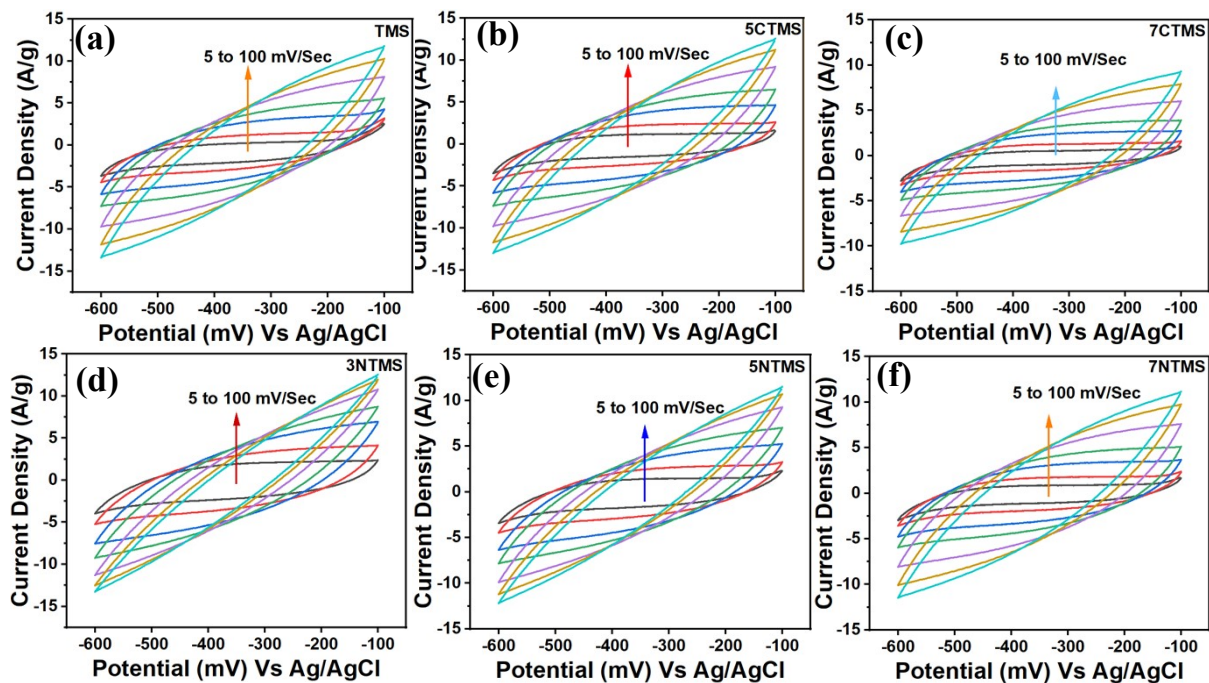
Fig. S7 CV curves at scan rates from 5 to 100 mV/sec of (a) bare sulphonated Ti$_3$C$_2$T$_x$, (b) 5 wt% CoFe$_2$O$_4$ intercalated sulphonated Ti$_3$C$_2$T$_x$, (c) 7 wt% CoFe$_2$O$_4$ intercalated sulphonated Ti$_3$C$_2$T$_x$, (d) 3NTMS, (e) 5 wt% NiFe$_2$O$_4$ intercalated sulphonated Ti$_3$C$_2$T$_x$ and 7 wt% NiFe$_2$O$_4$ intercalated sulphonated Ti$_3$C$_2$T$_x$.
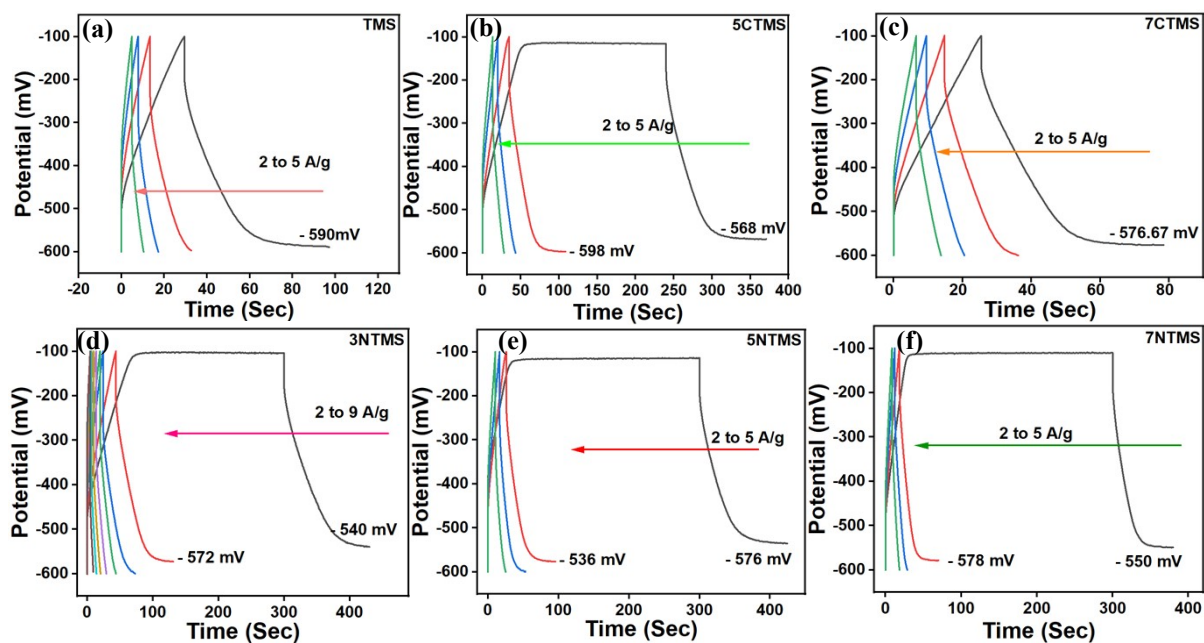
Fig. S8 GCD curves at various current densities of (a) Sulphonated $Ti_3C_2T_x$, (b) 5 wt% $CoFe_2O_4$ intercalated sulphonated $Ti_3C_2T_x$, (c) 7 wt% $CoFe_2O_4$ intercalated sulphonated $Ti_3C_2T_x$, (d) 3NTMS, (e) 5 wt% $NiFe_2O_4$ intercalated sulphonated $Ti_3C_2T_x$ and (f) 7 wt% $NiFe_2O_4$ intercalated sulphonated $Ti_3C_2T_x$.
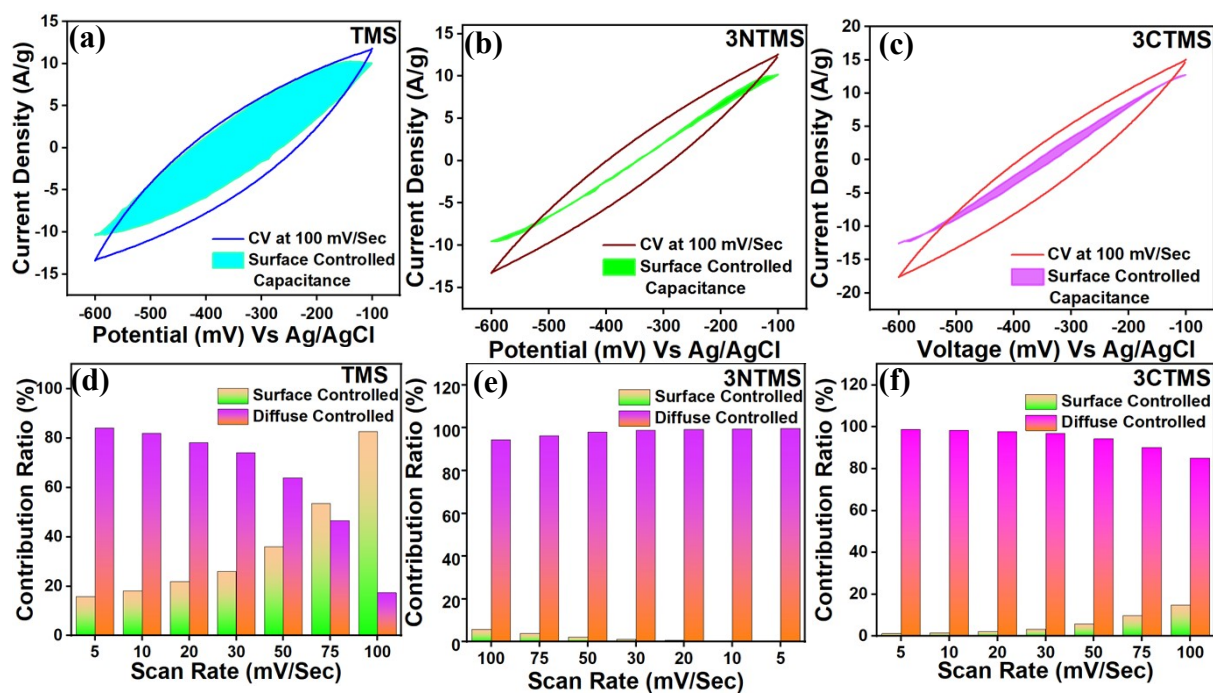
Fig. S9 Surface controlled capacitance in the total electrochemical response of (a) bare sulphonated $Ti_3C_2T_x$, (b) 3 wt% $NiFe_2O_4$ intercalated sulphonated $Ti_3C_2T_x$, and (c) 3 wt% $CoFe_2O_4$ intercalated sulphonated $Ti_3C_2T_x$. Surface and diffusion-controlled behaviour at different scan rates for (d) bare sulphonated $Ti_3C_2T_x$, (e) 3 wt% $NiFe_2O_4$ intercalated sulphonated $Ti_3C_2T_x$, and (f) 3 wt% $CoFe_2O_4$ intercalated sulphonated $Ti_3C_2T_x$.
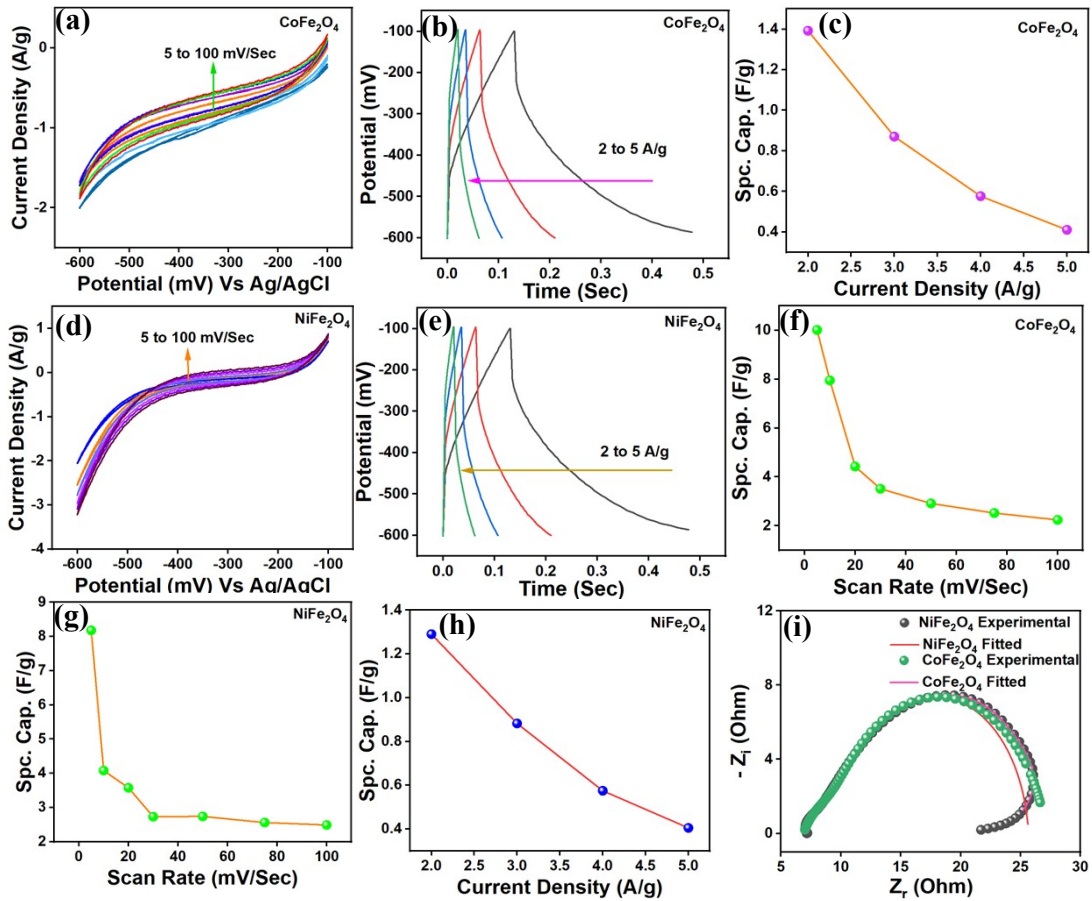
Fig. S10 Electrochemical response of CoFe$_2$O$_4$: (a) CV curves, (b) GCD curves, (c) current density retention, (f) scan rate retention curves., Electrochemical response of NiFe$_2$O$_4$: (d) CV curves, (e) GCD curves, (g) scan rate retention and (h) current density retention curves. (i) EIS spectra and fitted curves for both CoFe$_2$O$_4$ and NiFe$_2$O$_4$.
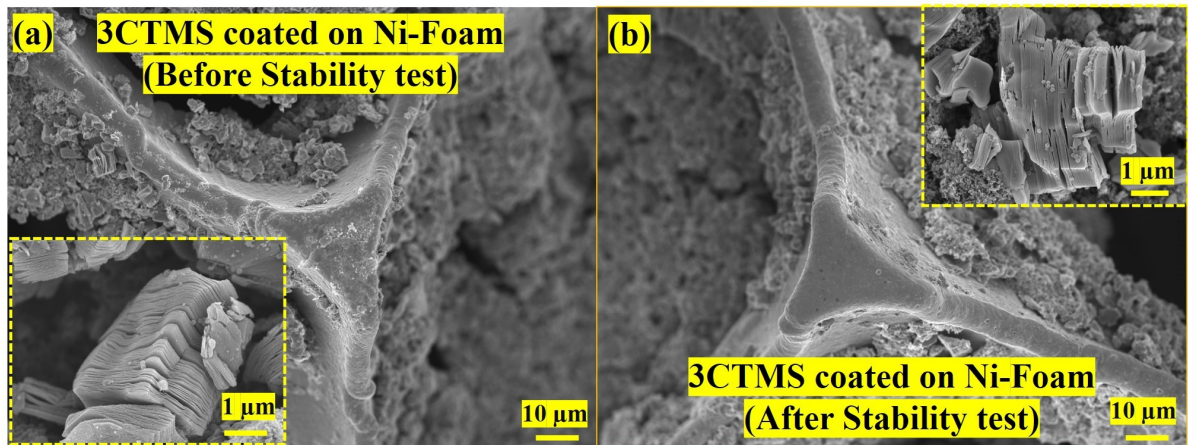
Fig. S11 FESEM images of 3 wt% $CoFe_2O_4$ intercalated in multilayered sulphonated $Ti_3C_2T_x$ MXene coated on Ni foam (a) before and (b) after the CV stability test after 10,000 cycles.

    Fig. S11a shows the active sample 3CTMS coated onto the surface of Ni- foam before starting the CV cycling stability test. The FESEM image shows the uniform coating of 3CTMS across the Ni foam surface at 10 µm magnification. The inset image in **Fig. S11a** shows the 3CTMS layered sulphonated layered surface. The decline in specific capacitance obtained in cyclic stability study can be attributed to the fact of electrolyte ion saturation at the interface of electrode and electrolyte.[11] The integrity and stable layers of the sulphonated MXene sheets can be observed in Fig. S11b (inset). This demonstrates the effectiveness in addressing the mitigation of restacking issue in $Ti_3C_2T_x$ layered MXene.

Table S2. Specific capacitance of CFO, NFO, TMS, (3,5,7 wt%) CTMS and (3,5,7 wt%) NTMS at various scan rates and current densities

Materials		Scan rate (mV/sec)							Current Density (A/g)			
		5	10	20	30	50	75	100	2	3	4	5
TMS		303	265	219	185	133	89	63	338	116	76	55
CFO		10	7	4	3.5	2.9	2.5	2.2	1.39	0.87	0.57	0.41
NFO		8.17	4.08	3.5	2.74	2.73	2.5	2.4	1.29	0.88	0.56	0.40
CTMS (TMS+CFO)	3 wt%	593	490	338	237	131	76	50	620	450	390	267
	5 wt%	377	322	244	200	131	83	57	585	442	190	151
	7 wt%	223	201	170	146	110	79	58	219	128	88	72
NTMS (TMS+NFO)	3 wt%	567	423	277	186	100	56	37	591	527	356	244
	5 wt%	412	341	239	180	107	63	43	648	534	294	38
	7 wt%	278	246	204	173	124	84	59	362	290	135	22

Table S3. Fitted Equivalent Circuit Parameters of TMS and different percent CFO and NFO based electrode

Parameters	TMS	3CTMS	3NTMS	5CTMS	5NTMS	7CTMS	7NTMS
R_s	4.06	4.35	4.59	4.87	5.08	4.91	5.23
R_{ct1}	3.76E10	1.36	5.58	14.29	0.61	13.25	2.06
Q_1-Yo	0.326	0.613	0.409	0.8382	0.301	0.48	0.313
Q_1-n	1.021	0.38	0.76	0.359	1.54	15.16	2.56
R_{ct2}	10.13	10.76	12.12	17.41	11.01	27.91	25.9
Q_2-Yo	13.5	34.62	260.5	5.886	80.2	410.9	154.36
Q_2-n	0.366	0.836	0.605	0.343	0.662	0.999	0.879

Table S4. Surface and diffusion-controlled behaviour of TMS, 3CTMS and 3NTMS at various scan rates

Scan Rate (mV/sec)	TMS		3NTMS		3CTMS	
	Surface Controlled capacitance	Diffusion Controlled capacitance	Surface Controlled capacitance	Diffusion Controlled capacitance	Surface Controlled capacitance	Diffusion Controlled capacitance
100	82.67	17.32	5.72	94.28	14.84	85.15
75	53.47	46.52	3.77	96.23	9.87	90.15
50	36.03	63.96	2.11	97.89	5.72	94.27
30	25.91	74.08	1.13	98.87	3.15	96.84
20	21.83	78.16	0.76	99.24	2.21	97.78
10	18.03	81.96	0.49	99.51	1.52	98.47
5	15.77	84.22	0.37	99.63	1.26	98.73

Table S5. Electrochemical performance comparison table of 3CTMS and 3NTMS electrode

Sl. No.	Material	Method for making composite	Sulphonation	Electrolyte	Specific Capacitance	Stability	References
1	NiCo$_2$_LDH@MXene/ rGO	Hydrothermal	No	2 M KOH	332.2 mAh/g at 1 A/g	87.5% after 5,000 cycles	[12]
2	MnFeO$_3$_MXene	Hydrothermal	No	1 M KOH	1077 F/g	96 % after 3,000 cycles	[13]
3	LaMnO$_{3-\delta}$_MXene	Stirring	No	3 M KOH	442.8 F/g at 3 A/g	93.5% after 5,000 cycles	[14]
4	CoFe$_2$O$_4$_MXene	Sonication Mixing (CoFe$_2$O$_4$(90) : Ti$_3$C$_2$T$_x$ MXene (10))	No	0.1 M KOH	1268.75 F/g at 1 A/g	97 % after 5,000 cycles	[15]
5	Boron Nitride_ MXene_WS$_2$	Hydrothermal	No	1 M KOH	1318 F/g at 1 A/g	84% after 10,000 cycles.	[16]
6	Ag$_2$CrO$_4$_MXene	Sonication	No	0.1 M H$_2$SO$_4$	525 F/g at 10 mV/sec	-	[17]
7	rGO_MXene	Sonication	No	PVA- H$_2$SO$_4$	140 F/g at 1 A/g	85 % after 10,000 cycles.	[18]
8	MnO$_2$_MXene_C C	Hydrothermal	No	3 M KOH	511 F/g at 1 A/g	83% after 10,000 cycles	[19]
	MnO$_2$_MXene	Hydrothermal	No	0.5 M K$_2$SO$_4$	242 F/g at 1 A/g	97% after 5000 cycles	[20]
9	1T_MoS$_2$_MXene	Hydrothermal	No	PVA-H$_2$SO$_4$	386.7 F/g at 1 A/g	91 % after 20,000 cycles	[21]
10	MXene_rGO	Sonication Mixing	No	3 M H$_2$SO$_4$	329.9 F/g at 5 mV	90% after 40,000 cycles	[22]

11	MXene_BaTiO$_3$	Sonication Mixing	No	0.1 M H$_2$SO$_4$	254.28F/g at 1 A/g	74% after 10,000 cycles.	[23]
12	3NTMS (3% NiFe2O4-Ti$_3$C$_2$T$_X$)	**Sonication Mixing**	**Yes**	**0.1 M H$_2$SO$_4$**	**567.422 F/g at 5 mV**	**93.29 % 5,000 cycles. 80.65 % after 10,000 cycles.**	**Present Work**
13	3CTMS (3% CoFe2O4-Ti$_3$C$_2$T$_X$)	**Sonication Mixing**	**Yes**	**0.1 M H$_2$SO$_4$**	**593.81 F/g at 5 mV**	**95.9 % 5,000 cycles. 81.75 % after 10,000 cycles.**	**Present Work**

Theoretical Procedure and Findings-

The Quantum ESPRESSO electronic package was utilized to perform geometry optimization on Ti$_3$C$_2$ MXene and sulphonated composite systems using density functional theory (DFT).[24] Exchange-correlation effects were accounted for using the generalized gradient approximation (GGA) with Perdew−Burke−Ernzerhof (PBE) and ultrasoft pseudopotentials from the PSLibrary.[25] A kinetic energy cutoff of 25 Ry and a charge density cutoff of 225 Ry were applied for the plane-wave expansion. The Brillouin zone was sampled using a 9 × 9 × 1 uniform Monkhorst−Pack k-point mesh, and the Broyden−Fletcher−Goldfarb−Shanno (BFGS) algorithm was employed for atomic structure relaxation with a convergence threshold set at a residual force of 10^{-4} Ry/Å.[26,27] After structure relaxation, the generalized gradient approximation of Perdew−Burke Ernzerhof (GGA-PBE96) was adopted in NanoDecal to extract the bandgap and density of states (DOS). Double zeta with polarisation (DZP) basic sets and non-conserving pseudopotentials were employed with a 225 Ry cutoff for the real-space grid. In the Non-Equilibrium Green's Function (NEGF)-DFT analysis, physical quantities and the NEGF were expanded using a double-ζ polarized atomic orbital basis and a Monkhorst−Pack mesh of 9 x 9 x 1 for k-points sampling. **Fig S12a** shows the super cell used for Ti$_3$C$_2$ MXene. The electronic band structures and DOS for

pristine Ti_3C_2 MXene are presented in **Fig. S12b** and **c,** respectively.[28] To study the band structural modification after sulphonation, $-SO_3^{2-}$ group was added and tested as indicated in **Fig S12d**. **Fig S12e** shows the generation of new electronics bands in sulphonated MXene, accompanied by an increase in states at energy levels near -10, -3 and 2.3 eV (**Fig. S12f**), attributed to the enhanced conductive sites compared to pristine MXene. The incorporation of a $CoFe_2O_4$ lattice into sulphonated MXene was modelled by constructing the supercell depicted in **Fig. S12g**. Further increase in number of bands in the conduction band region can be observed in **Fig. S12h** and **i**. The calculated band gaps for pristine Ti_3C_2 MXene, sulphonated MXene (TMS) and $CoFe_2O_4$ incorporated TMS were 3.404 eV, 3.196 eV and 3.667 eV, respectively. In the present work, TMS and various (3, 5, 7) wt % $CoFe_2O_4$ incorporated in TMS are studied for the electrochemical energy storage. Higher band gap materials demonstrate superior electrochemical and thermal stability, which supports reversible redox reactions over extended cycles and improves overall charge storage capability. [29] The observed increase in band gap for $CoFe_2O_4$ incorporated TMS can be attributed due to the addition of the $-SO_3^{2-}$ functional group, which increases the active sites for electrolyte ion interactions.[30] The theoretical analysis demonstrates that the synergetic effect of $CoFe_2O_4$ incorporation in TMS contributes to improved charge storage performance.
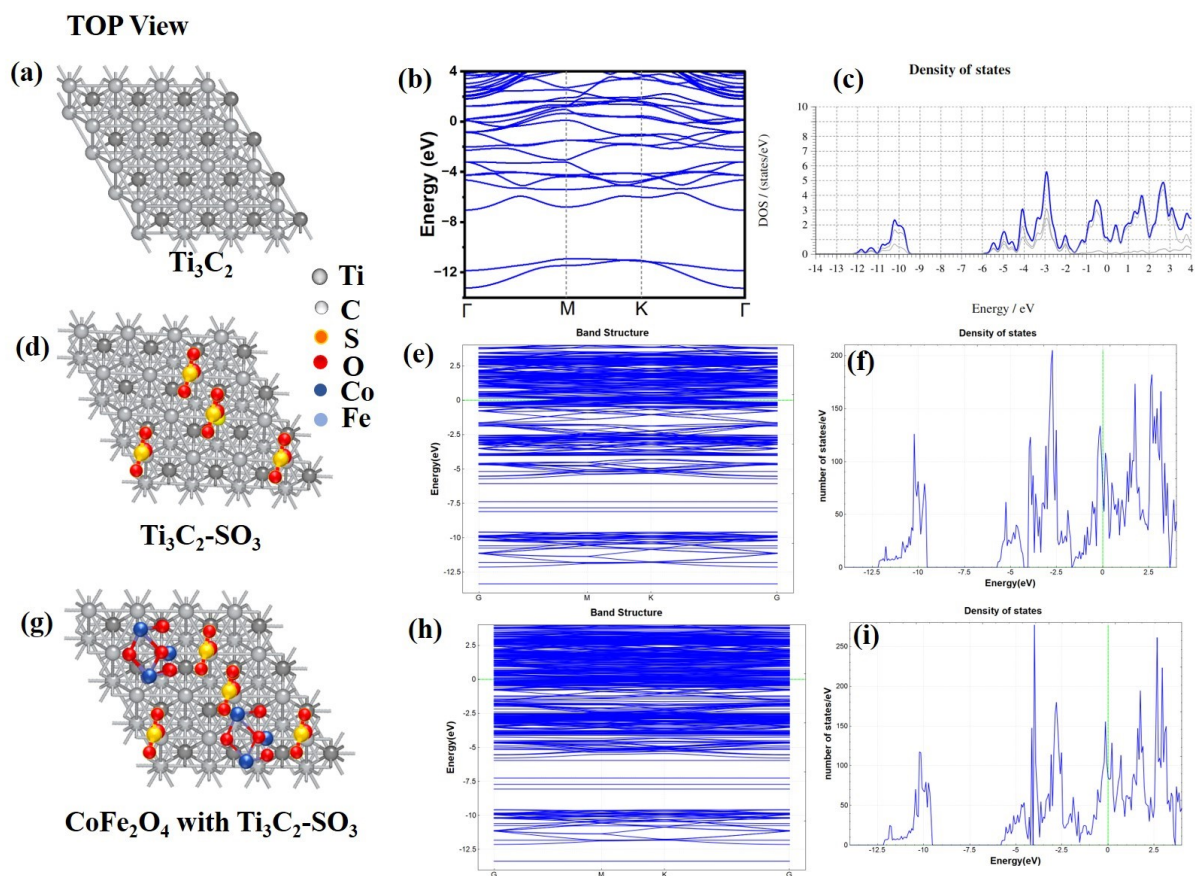
Fig. S12 (a) Top view image, (b) Electronic band structure and (c) DOS of Ti_3C_2 MXene super cell used for calculation, (d) Top view image, (e) Electronic band structure and (f) DOS of Ti_3C_2 sulphonated MXene super cell used for calculation, (g) Top view image, (h) Electronic band structure and (i) DOS of single $CoFe_2O_4$ attached to Ti_3C_2 sulphonated MXene super cell used for calculation.

Video :-
https://drive.google.com/drive/folders/1WyLhB8N33qkHZNprj_3wgEb8cbu-sYmf?usp=sharing

References

1   H. Ahmad, A. A. Kamely, N. Yusoff, L. Bayang and M. Z. Samion, *Sci. Rep.*, 2020, **10**, 1–11.

2   A. M. Jastrzębska, A. Szuplewska, A. Rozmysłowska-Wojciechowska, M. Chudy, A. Olszyna, M. Birowska, M. Popielski, J. A. Majewski, B. Scheibe, V. Natu and M. W. Barsoum, *2D Mater.*, , DOI:10.1088/2053-1583/ab6a60.

3   W. Y. Chen, X. Jiang, S. N. Lai, D. Peroulis and L. Stanciu, *Nat. Commun.*, 2020, **11**, 1–10.

4   M. Yu, Z. Feng, Y. Huang, K. Wang and L. Liu, *J. Mater. Sci. Mater. Electron.*, 2019, **30**, 4174–4183.

5   Z. Hou, C. Liu, J. Gong, J. Wu, S. Sun, M. Zhang and X. Sun, *Coatings*, , DOI:10.3390/coatings12101532.

6   N. Dalai, B. Mohanty, A. Mitra and B. Jena, *ChemistrySelect*, 2019, **4**, 7791–7796.

7   R. S. Yadav, I. Kuritka, J. Vilcáková, M. Machovský, D. Škoda, P. Urbánek, M. Masar, M. Goralik, M. Urbánek, L. Kalina and J. Havlica, *Nanomaterials*, , DOI:10.3390/nano9040621.

8   M. Hua, L. Xu, F. Cui, J. Lian, Y. Huang, J. Bao, J. Qiu, Y. Xu, H. Xu, Y. Zhao and H. Li, *J. Mater. Sci.*, 2018, **53**, 7621–7636.

9   R. Wang, Y. Wang, C. Wu, T. Zhai, J. Yang, B. Sun, S. Duhm and N. Koch, *Adv. Funct. Mater.*, , DOI:10.1002/adfm.201903440.

10   X. Niu, Y. Chen and H. Hu, *Membranes (Basel).*, 2022, **12**, 4–13.

11   N. Kumar, S. Bin Kim, S. Y. Lee and S. J. Park, *Nanomaterials*, , DOI:10.3390/nano12203708.

12   J. Zheng, X. Pan, X. Huang, D. Xiong, Y. Shang, X. Li, N. Wang, W. M. Lau and H. Y. Yang, *Chem. Eng. J.*, 2020, **396**, 125197.

13   Z. A. Sheikh, D. Vikraman, H. Kim, S. Aftab, S. F. Shaikh, F. Shahzad, J. Jung, H. S. Kim, S. Hussain and D. K. Kim, *J. Energy Storage*, 2024, **81**, 110342.

14   A. K. Tomar, T. Kshetri, N. H. Kim and J. H. Lee, *Energy Storage Mater.*, 2022, **50**, 86–95.

15   I. Ayman, A. Rasheed, S. Ajmal, A. Rehman, A. Ali, I. Shakir and M. F. Warsi, *Energy and Fuels*, 2020, **34**, 7622–7630.

16   S. De, S. Acharya, C. K. Maity and G. C. Nayak, *ACS Appl. Nano Mater.*, 2023, **6**, 11175–11186.

17   T. Yaqoob, M. Rani, A. Mahmood, R. Shafique, S. Khan, N. K. Janjua, A. A. Shah, A. Ahmad and A. A. Al-Kahtani, *Materials (Basel).*, , DOI:10.3390/ma14206008.

18   Y. Zhou, K. Maleski, B. Anasori, J. O. Thostenson, Y. Pang, Y. Feng, K. Zeng, C. B. Parker, S. Zauscher, Y. Gogotsi, J. T. Glass and C. Cao, *ACS Nano*, 2020, **14**, 3576–3586.

19   H. Zhou, Y. Lu, F. Wu, L. Fang, H. J. Luo, Y. X. Zhang and M. Zhou, *J. Alloys Compd.*, 2019, **802**, 259–268.

20   Q. Wang, Z. Zhang, Z. Zhang, X. Zhou and G. Ma, *J. Solid State Electrochem.*, 2019, **23**, 361–365.

21   X. Wang, H. Li, H. Li, S. Lin, W. Ding, X. Zhu, Z. Sheng, H. Wang, X. Zhu and Y. Sun, *Adv. Funct. Mater.*, 2020, **30**, 1–11.

22   J. Miao, Q. Zhu, K. Li, P. Zhang, Q. Zhao and B. Xu, *J. Energy Chem.*, 2021, **52**, 243–250.

23   J. Pani and H. Borkar, *J. Electroanal. Chem.*, 2024, **956**, 118092.

24   P. Giannozzi, S. Baroni, N. Bonini, M. Calandra, R. Car, C. Cavazzoni, D. Ceresoli, G. L. Chiarotti, M. Cococcioni, I. Dabo, A. Dal Corso, S. De Gironcoli, S. Fabris, G. Fratesi, R. Gebauer, U. Gerstmann, C. Gougoussis, A. Kokalj, M. Lazzeri, L. Martin-

Samos, N. Marzari, F. Mauri, R. Mazzarello, S. Paolini, A. Pasquarello, L. Paulatto, C. Sbraccia, S. Scandolo, G. Sclauzero, A. P. Seitsonen, A. Smogunov, P. Umari and R. M. Wentzcovitch, *J. Phys. Condens. Matter*, 2009, **21**, 395502.

25   J. P. Perdew, K. Burke and M. Ernzerhof, *Phys. Rev. Lett.*, 1996, **77**, 3865–3868.

26   H. J. Monkhorst and J. D. Pack, *Phys. Rev. B*, 1976, **13**, 5188.

27   S. R. Billeter, A. J. Turner and W. Thiel, *Phys. Chem. Chem. Phys.*, 2000, **2**, 2177–2186.

28   Y. Peng, P. Cai, L. Yang, Y. Liu, L. Zhu, Q. Zhang, J. Liu, Z. Huang and Y. Yang, *ACS Omega*, 2020, **5**, 26486–26496.

29   M. R. Islam, N. Farzana, M. R. Akhond, M. Rahaman, M. J. Islam and I. M. Syed, *Mater. Adv.*, 2024, **5**, 2491–2509.

30   S. Saha, M. Jana, P. Khanra, P. Samanta, H. Koo, N. Chandra Murmu and T. Kuila, *RSC Adv.*, 2016, **6**, 1380–1387.